Cell Property Determination from the Acoustic Microscope Generated Voltage Versus Frequency Curves

T. Kundu,* J. Bereiter-Hahn,† and I. Karl†

*Department of Civil Engineering and Engineering Mechanics, University of Arizona, Tucson, Arizona 85721 USA, and †Kinematic Cell Research Group, Biocentre, J. W. Goethe University, D 60439 Frankfurt am Main, Germany

ABSTRACT Among the methods for the determination of mechanical properties of living cells acoustic microscopy provides some extraordinary advantages. It is relatively fast, of excellent spatial resolution and of minimal invasiveness. Sound velocity is a measure of the stiffness or Young's modulus of the cell. Attenuation of cytoplasm is a measure of supramolecular interactions. These parameters are of crucial interest for studies of cell motility, volume regulations and to establish the functional role of the various elements of the cytoskeleton. Using a phase and amplitude sensitive modulation of a scanning acoustic microscope (Hillman et al., 1994, *J. Alloys Compounds.* 211/212:625–627) longitudinal wave speed, attenuation and thickness profile of a biological cell are obtained from the voltage versus frequency or V(f) curves. A series of pictures, for instance in the frequency range 980–1100 MHz with an increment of 20 MHz, allows the experimental generation of V(f) curves for each pixel while keeping the lens-specimen distance unchanged. Both amplitude and phase values of the V(f) curves are used for obtaining the cell properties and the cell thickness profile. The theoretical analysis shows that the thin liquid layer, between the cell and the substrate, has a strong influence on the reflection coefficient and should not be ignored during the analysis. Cell properties, cell profile and the thickness of the thin liquid layer are obtained from the V(f) curves by the simplex inversion algorithm. The main advantages of this new method are that imaging can be done near the focal plane, therefore an optimal signal to noise ratio is achieved, no interference with Rayleigh waves occurs, and the method requires only an approximate estimate of the material properties of the solid substratum where the cells are growing on.

INTRODUCTION

Determination of the mechanical properties of living cells is a difficult task. Investigators tried different techniques for this purpose. For a review of older methods one is referred to Hiramoto (1987). These methods include local aspiration of cytoplasm with a pipette (Schmid-Schönbin, 1990), local poking of cytoplasm (Duszyk et al., 1989), magnetometry (Ziemann et al., 1994), or scanning force microscopy (e.g., Hassan et al., 1998; Radmacher et al., 1996). In all of these methods the forces needed to evoke a certain deformation are measured and thus allow the determination of elastic and viscous properties from stress-strain relationships and the dependence of these relations on the frequency of oscillating stress applications. Among the methods for the determination of mechanical properties of living cells, acoustic microscopy provides some extraordinary advantages: it is relatively fast, it provides excellent spatial resolution, and it is minimally invasive. Relative changes in cytoplasmic forces may be resolved with a time resolution of ~5 s (Bereiter-Hahn and Lüers, 1994, 1998), and exact determination of mechanical properties requires a series of five or six images requiring an acquisition time between 25 and 30 s at a resolution of 512 × 256 pixels. Spatial resolution is in the range of 3 μm^2. Viscoelastic properties, however, may not change over such very small areas. The minimal invasiveness results from the very-high-frequency ultrasound (GHz range), which does not cause any damage or disturbance of the cells (Bereiter-Hahn, 1995). The only effect that has to be considered is the oscillating shear force caused by the scanning movement of the acoustic lens, which is coupled with the specimen via the culture medium. The main parameters obtained with an acoustic microscope are sound velocity and sound attenuation, as well as the dimensions of the cell. Sound velocity is a measure of the compression modulus, which is related to Young's modulus and Poisson's ratio. Attenuation of cytoplasm is a measure of the supramolecular interactions (Wagner et al., manuscript in preparation).

Previous approaches to the computation of tissue properties have been based on shear wave propagation (Sarvazyan et al., 1992) or on measurements of the reflected sound as a function of focus position ($V(z)$ curves) (e.g., Sasaki et al., 1996). The computation of cell properties from acoustic microscope-generated signals required an estimation of the cell thickness profile (Hildebrand et al., 1981; Hildebrand and Rugar, 1984; Litniewski and Bereiter-Hahn, 1990, 1992; Kundu et al., 1991, 1992). The cell profile is traditionally computed by counting the interference rings and estimating the value of the longitudinal wave speed in the cell. Kundu et al. (1991, 1992) used this information to get a rough estimate of the probable upper and lower bounds of the cell thickness at different pixels or cell positions. Then they adopted a simplex inversion algorithm to predict the cell thickness accurately, along with other cell parameters. However, they used the $V(z)$ curve or voltage (V)

Received for publication 5 November 1999 and in final form 10 February 2000.

Address reprint requests to Dr. T. Kundu, Department of Civil Engineering and Engineering Mechanics, University of Arizona, Tucson, AZ 85721. Tel.: 520-621-6573; Fax: 520-621-2550; E-mail: tkundu@u.arizona.edu.

0006-3495/00/05/2270/10 $2.00

versus defocus distance distance (z) curve, generated by an acoustic microscope operating at 1-GHz frequency to compute the cell properties. A new transducer geometry was proposed by Chubachi and co-workers (1992) to be combined with a defocusing series in the range of about one wavelength in water to obtain $V(z)$ curves for each point in a biological sample. In this paper cell properties are obtained from the $V(f)$ curves. $V(z)$ curves have several disadvantages when compared with the $V(f)$ curves:

$V(z)$ curves can be generated only if the cells are attached to solid substrates that give rise to Rayleigh waves at the angles of incidence provided by the lens, and the surface waves must not be severely attenuated. The materials giving optimal $V(z)$ characteristics may not be the best materials for growing cells. In addition, our aim of following the mechanical responses of cells prone to passive mechanical deformations requires cells grown on rubber surfaces. These do not allow appropriate $V(z)$ imaging because of surface wave attenuation.

It is more time consuming and less accurate to change the defocus distance z when compared with monitoring of the signal frequency f.

Image quality is best at the focus position ($z = 0$); its quality deteriorates as the defocus distance z increases. On the other hand, the image quality is not significantly affected by the change in the signal frequency if the specimen is kept at the focus position ($z = 0$).

As a result $V(f)$ curves preferred to $V(z)$ curves. They provide a basis for the investigation of cellular behavior on stretchable materials, using acoustic microscopy (Karl and Bereiter-Hahn, 1999). The method of investigating cells on silicon rubber was introduced by Harris (Harris, 1982; Harris et al., 1980).

$V(f)$ curves have recently been used by materials scientists for characterizing horizontally and vertically layered materials (Nagy and Adler, 1990; Ghosh et al., 1997).

THEORY AND NUMERICAL RESULTS

One distinctive feature of $V(f)$ curves for cell property determination and image generation with the specimen placed at the focus is that the surface-skimming Rayleigh waves are not generated in the specimen. Hence the theoretical model for the $V(z)$ curve synthesis that assumes the presence of surface-skimming Rayleigh waves at the coupling fluid-specimen interface cannot be used for $V(f)$ curve synthesis. New theoretical models for $V(f)$ curve synthesis are being developed from the normal reflection of plane waves by homogeneous and layered half-spaces.

Theory of normal reflection by layered structures

An acoustic microscope lens generates a conically converging ultrasonic beam, shown by the dashed line in Fig. 1. In reality, the converging beam (shown by the *dotted line*) generated by the concave lens is far from being an ideal cone. Near the concave lens its shape is close to the base of a cone; however, near the focal point its shape is close to a cylinder. As a result, if the reflecting surface is placed at a large defocus position, as shown by the dashed line (delineating the surface), leaky Rayleigh waves can be generated at the fluid-solid interface if the half-lens angle is greater than the Rayleigh critical angle. However, when it is placed near the focal point (F), as shown by the solid line, the normally incident cylindrically shaped ultrasonic beam cannot generate Rayleigh waves at the reflecting surface. Hence, if the specimen is placed near the focal plane, then the reflected signal is composed of only the normally reflected rays. To synthesize these reflected signals, one needs to study the plane wave reflection coefficients for different fluid/solid structures. These are presented here. In these derivations the incident beam is assumed to be normal to the reflecting surface, because in our experiments the acoustic microscope-generated ultrasonic beam strikes the reflecting surface vertically.

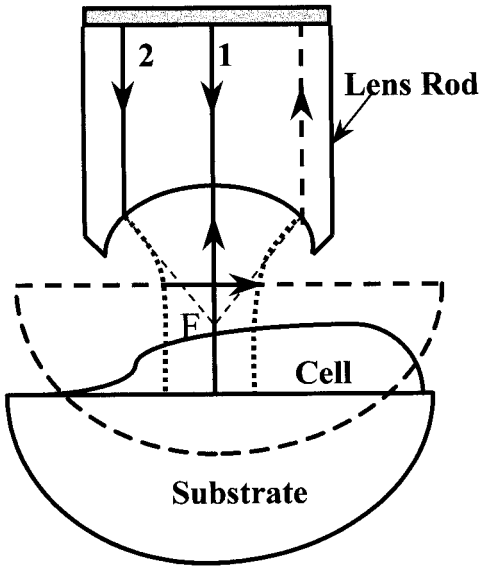

FIGURE 1 An acoustic microscope lens generates a conically converging ultrasonic beam, shown by the dotted line. The dashed line marks a focus position with the reflecting surface closer to the lens than its focal length. If waves are incident on the surface at an angle equal to or greater than the Rayleigh angle, then Rayleigh surface waves are induced as marked by the arrow in the plane of the substrate surface. For details see text.

Fluid half-space over a solid half-space (FS structure)

Fig. 2 *a* shows a plane longitudinal wave of amplitude 1 that is normally incident at the fluid-solid interface. If the reflected and transmitted wave amplitudes are denoted by R

and T, respectively, then the wave potentials at the fluid and solid half-spaces are given by

$$\begin{aligned}\phi_f &= e^{ik_f y} + R \cdot e^{-ik_f y} \\ \phi_s &= Te^{ik_s y}\end{aligned} \tag{1}$$

where the y coordinate is positive downward measured from the fluid-solid interface. $k_f\,(= 2\pi f/\alpha_f)$ and $k_s\,(= 2\pi f/\alpha_s)$ are wave numbers of the fluid and the solid, respectively. f is the signal frequency; α_f and α_s are longitudinal wave speeds in the fluid and the solid half-space, respectively. In Eq. 1 the time dependence $e^{-i\omega t}$ is implied and is not shown explicitly. One can compute the displacement and stress components from these potential functions in the following manner:

$$\begin{aligned}u &= \frac{\partial \phi}{\partial x} = 0 \\ v &= \frac{\partial \phi}{\partial y} \\ \sigma_{yy} &= (\lambda + 2\mu)\frac{\partial^2 \phi}{\partial y^2} \\ \tau_{xy} &= 0\end{aligned} \tag{2}$$

where u and v are horizontal and vertical components of displacement and σ and τ are normal and shear stress components. λ and μ are two elastic constants (Lame's first and second constants) of the elastic solid.

From the continuity of vertical displacement and stress components at the interface, after some algebraic manipulations, the Fresnel equations are derived:

$$\begin{aligned}R &= \frac{Z_s - Z_f}{Z_s + Z_f} \\ T &= \frac{2\rho_f \alpha_s}{Z_s + Z_f}\end{aligned} \tag{3}$$

where $Z_s\,(= \rho_s\alpha_s)$ and $Z_f\,(= \rho_f\alpha_f)$ are acoustic impedances of the solid and the fluid half-spaces, respectively. ρ_s and ρ_f are densities of the solid and the fluid, respectively.

Fluid over a layered half-space (FSS structure)

This structure is shown in Fig. 2 *b*. Wave potentials in the fluid half-space, solid layer, and solid half-space are denoted by the subscripts *f*, 1, and *s*, respectively:

$$\begin{aligned}\phi_f &= e^{ik_f y} + R \cdot e^{-ik_f y} \\ \alpha_1 &= ae^{ik_1 y} + be^{-ik_1 y} \\ \phi_s &= Te^{ik_s y}\end{aligned} \tag{4}$$

After the stress and displacement continuity conditions across the two interfaces (fluid-solid and solid-solid) are

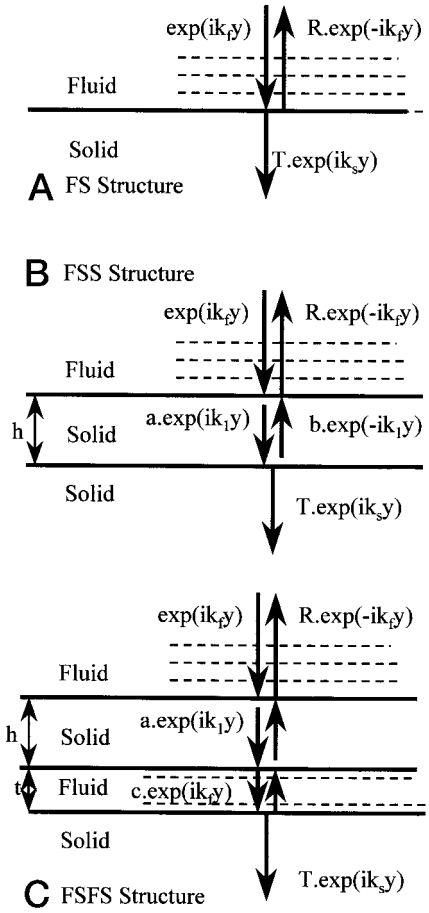

FIGURE 2 Reflection and transmission of normally incident longitudinal waves for different reflector geometries. (*a*) Reflection and transmission at a fluid/solid interface (FS-structure). (*b*) Reflection and transmission at a fluid/solid layer interface on a solid half-space (FSS-structure). h is the layer thickness. (*c*) Reflection and transmission at a fluid solid layer separated by a fluid layer from a solid half-space (FSFS-structure).

satisfied, the reflection coefficient R can be obtained as

$$R = 1 + \frac{2\alpha_{f1}\left[Q_1^2\dfrac{\alpha_{s1} - \rho_{1s}}{\alpha_{s1} + \rho_{1s}} - 1\right]}{(\alpha_{f1} - \rho_{1f})\left[\dfrac{\alpha_{f1} + \rho_{1f}}{\alpha_{f1} - \rho_{1f}} - Q_1^2\left(\dfrac{\alpha_{s1} - \rho_{1s}}{\alpha_{s1} + \rho_{1s}}\right)\right]} \tag{5}$$

where

$$\begin{aligned}\alpha_{f1} &= \frac{\alpha_f}{\alpha_1} \\ \alpha_{s1} &= \frac{\alpha_s}{\alpha_1} \\ \rho_{1f} &= \frac{\rho_1}{\rho_f} \\ \rho_{1s} &= \frac{\rho_1}{\rho_s} \\ Q_1 &= e^{ik_1 h}\end{aligned} \tag{6}$$

k_1 ($= 2\pi f/\alpha_1$) is the wave number of the solid layer between the fluid and the solid half-space and h is its thickness.

One solid and one liquid layers between fluid and solid half-spaces (FSFS structure)

The problem geometry for this arrangement is shown in Fig. 2 *c*. Wave potentials in the fluid half-space, solid layer, fluid layer, and solid half-space are denoted by subscripts *f*, 1, *fl*, and *s*, respectively:

$$\begin{aligned}\phi_f &= e^{ik_f y} + R \cdot e^{-ik_f y}\\ \phi_1 &= ae^{ik_1 y} + be^{-ik_1 y}\\ \phi_{fl} &= ce^{ik_f y} + de^{-ik_f y}\\ \phi_s &= Te^{ik_s y}\end{aligned} \tag{7}$$

Continuity of stress and displacements across the interface boundaries give six equations, which can be written in the following manner:

$$\begin{bmatrix} \frac{1}{\alpha_f} & \frac{1}{\alpha_c} & -\frac{1}{\alpha_c} & 0 & 0 & 0\\ -\rho_f & \rho_c & \rho_c & 0 & 0 & 0\\ 0 & \frac{Q_{c1}}{\alpha_c} & -\frac{1}{\alpha_c Q_{c1}} & -\frac{Q_{f1}}{\alpha_f} & \frac{1}{\alpha_f Q_{f1}} & 0\\ 0 & \rho_c Q_{c1} & \frac{\rho_c}{Q_{c1}} & -\rho_f Q_{f1} & -\frac{\rho_f}{Q_{f1}} & 0\\ 0 & 0 & 0 & \frac{Q_{f2}}{\alpha_f} & -\frac{1}{\alpha_f Q_{f2}} & -\frac{Q_{s2}}{\alpha_s}\\ 0 & 0 & 0 & \rho_f Q_{f2} & \frac{\rho_f}{Q_{f2}} & -\rho_s Q_{s2} \end{bmatrix} \begin{Bmatrix} R\\ a\\ b\\ c\\ d\\ T \end{Bmatrix} = \begin{Bmatrix} \frac{1}{\alpha_f}\\ \rho_f\\ 0\\ 0\\ 0\\ 0 \end{Bmatrix} \tag{8}$$

where

$$\begin{aligned} Q_{c1} &= e^{ik_1 h}\\ Q_{f1} &= e^{ik_f h}\\ Q_{f2} &= e^{ik_f (h+t)}\\ Q_{s2} &= e^{ik_s (h+t)}\end{aligned} \tag{8a}$$

In the above equation h and t correspond to the thickness of the top solid layer and the liquid layer beneath the solid layer, as shown in Fig. 2 *c*. k_1 ($= 2\pi f/\alpha_1$), k_f ($= 2\pi f/\alpha_f$), and k_s ($= 2\pi f/\alpha_s$) are wave numbers of the solid layer, fluid (layer and half-space), and the solid half-space, respectively. It should be mentioned here that for the normal wave incidence the longitudinal wave does not generate shear waves by mode conversion. Hence, mathematically solid and liquid layers behave in the same manner for this special case. However, normal stiffness and, hence, longitudinal wave speeds inside different layers and half-spaces are different.

The three structures (FS, FSS, FSFS) shown in Fig. 2 model the three regions of the problem geometry present when cells are attached to a solid substrate: the substrate under the coupling fluid (FS), the cell attached to the substrate and covered by the coupling fluid (FSS), and the cell and substrate, covered by the coupling fluid, with a thin liquid layer between the two (FSFS).

Theoretical computation of the *V*(*f*) curve

The steps for computing the $V(f)$ curve are identical to the steps followed by Kundu et al. (1991) to compute the $V(z)$ curve. $V(f)$ values are obtained from the product of three terms:

$$V(f) = p(f) \cdot R(f) \cdot \exp[2ik_f d] \tag{9}$$

In the above equation $p(f)$ is the pupil function, $R(f)$ is the reflection coefficient, $\exp[2ik_f d]$ is the wave propagation term, k_f is the wave number of the coupling fluid, and d is the distance between the microscope lens and the reflecting surface.

Computation of $R(f)$ has been described in detail in the above section. The pupil function $p(f)$ is assumed to be a quadratic function of the frequency f:

$$p(f) = a + bf + cf^2 \tag{9a}$$

The coefficients a, b, and c are obtained experimentally by matching the theoretical $V(f)$ values for the substrate with the experimental $V(f)$ values. The best matching is obtained by minimizing the error in a least-squares sense.

Numerical results for FS, FSS, and FSFS structures

Reflection coefficients given by Eqs. 3, 5, and 8 are numerically computed to study the effect of a thin liquid layer on the reflected wave amplitude. Such a liquid layer is often present between the cell and the substrate.

The intensity (R^2) of the reflected signal from a FS structure (plastic or silicon rubber immersed in water) calculated by Eq. 3 is independent of the signal frequency (*the line denoted by 0/0* in Fig. 3). This figure also shows the reflected wave intensity for a FSS structure (Eq. 5) consisting of a 5-μm-thick cell directly attached to the substrate (*the line denoted by 5/0*). The first number (5) denotes the cell thickness in microns, and the second number (0) denotes the liquid layer thickness between the cell and the

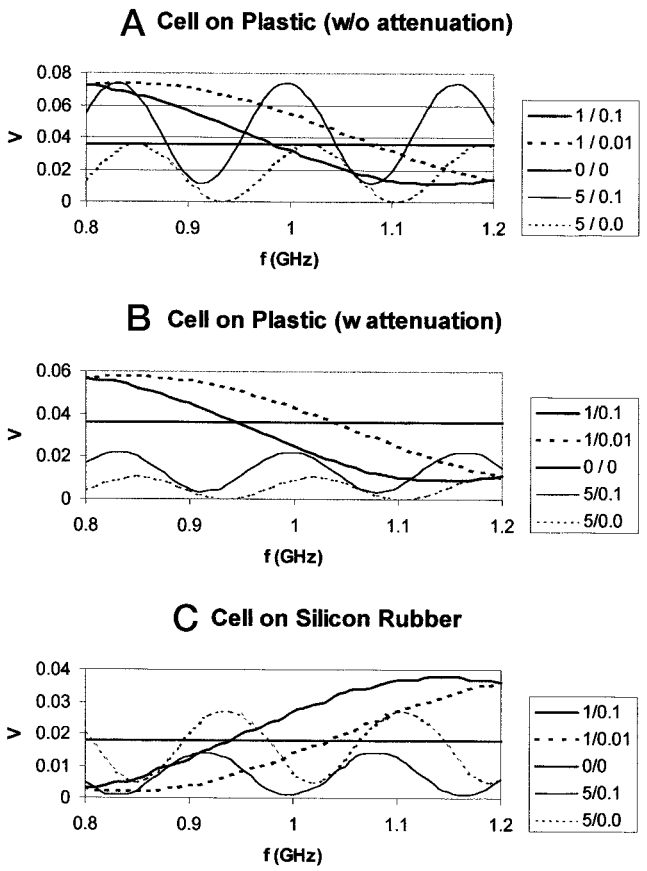

FIGURE 3 Reflected wave intensity (R^2) as a function of the signal frequency for different fluid/solid structures. (*a*) Plastic substrate. The results are generated by ignoring the material attenuation. (*b*) Plastic substrate. Attenuation has been considered for this calculation. (*c*) Silicon rubber substrate. 0/0, fluid/solid half space interface; 5/0, 5-μm-thick cell over solid substratum; 1/0.1, 1-μm-thick cell over 0.1-μm fluid layer over substratum; 1/0.01, 1-μm-thick cell over 0.01-μm fluid layer over substratum; 5/0.1, 5-μm-thick cell over 0.1-μm fluid layer over substratum. For material parameters and a detailed description see text.

substrate. Two types of substrates have been considered; these are plastic (Fig. 3, *a* and *b*) and silicon rubber (Fig. 3 *c*). Fig. 3 *a* shows R^2 in the absence of any attenuation in the cell or in the liquid; however, Fig. 3, *b* and *c*, considers a constant attenuation in the material within the frequency range of interest. The reflected wave intensities from three FSFS structures are shown by the remaining three lines, 5/0.1, 1/0.1, and 1/0.01, in Fig. 3. These three lines correspond to a 5-μm-thick cell over a 0.1-μm-thick fluid layer (5/0.1), a 1-μm-thick cell over a 0.1-μm-thick fluid layer (1/0.1), and a 1-μm-thick cell over a 0.01-μm-thick fluid layer (1/0.01). It is important to realize that as soon as a thin fluid layer is introduced beneath the cell, the reflected wave intensity changes significantly. It increases by almost 100% for the plastic substrate and decreases for the silicon rubber substrate. The material properties for these computations are given in Table 1.

TABLE 1 Properties of coupling fluid, cell, plastic, and silicon rubber for numerical computation

Material	P-wave speed (km/s)	Density (gm/cm^3)	Attenuation
Coupling fluid	1.5	1.0	0.03
Cell	1.7	1.05	0.09
Plastic	2.0	1.1	—
Silicon rubber	1.04	1.1	—

As mentioned above, the results presented in Fig. 3 *a* have been calculated by ignoring all attenuations. One can see from Fig. 3, *a* and *b*, that the attenuation decreases the reflected wave intensity. The amount of decrease should be greater for the thicker cell. Fig. 3 *b* shows the reflected wave intensities for the five cases of Fig. 3 *a*; the only difference is that in Fig. 3 *b* the attenuation is considered and in Fig. 3 *a* it is ignored. Note that for both plastic and silicon rubber substrates for some frequencies, the reflected wave intensity from a 1-μm-thick cell adhering to a solid substrate becomes larger than the reflected wave intensity from the substrate if a thin fluid layer is present beneath the cell. However, the reflected signal intensity from the 5-μm-thick cell is lower than that from the plastic substrate in the absence or presence of the fluid layer; however, it can be larger than the intensity of the reflected signal from the substrate for the silicon rubber substrate. Hence, in a gray-scale image the thin cell region may appear brighter than the substrate, thus indicating the presence of a thin fluid layer beneath the cell. The thick cell region, however, might appear darker than a surrounding cell-free area, although it may be separated from the substratum by a thin layer of fluid.

Estimating cell thickness and wave speed from amplitude and phase values

Fig. 4 shows three possible ray paths in a FSS structure. These three ray paths are numbered 1, 2, and 3. Ray 1 is reflected from the top of the cell, ray 2 is reflected from the coupling fluid/substrate interface, and ray 3 is reflected

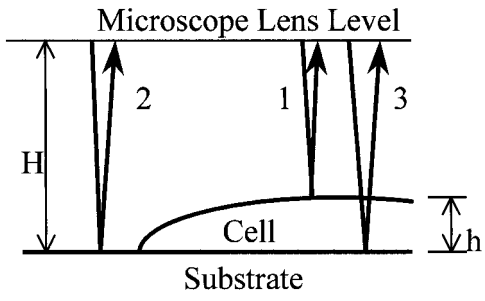

FIGURE 4 Schematic representation of the three possible ray paths contributing to image generation of a cell on a solid substratum. For further explanation see text.

from the bottom of the cell, at the cell/substrate interface. The phase change (measured in radians) of ray 2 during its travel between the acoustic microscope lens and the substrate is given by

$$\phi_2 = 2k_f H \tag{10}$$

The phase change of ray 1, which is reflected from the top of the cell, is

$$\phi_1 = 2k_f(H - h) \tag{11}$$

and the phase change of ray 3, reflected from the substrate after going through a cell of thickness h, is given by

$$\phi_3 = 2k_f(H - h) + 2k_c h \tag{12}$$

where k_f is the wave number of the coupling fluid and k_c is the wave number of the cell. Note that for a cell on a silicon, plastic, or glass substrate, ray type 3 is much stronger than ray type 1, because the impedance difference between water (or culture medium) and the cell is much smaller than the impedance difference between the cell and the substrate. If the phase is measured relative to the phase of the substrate (in other words, if the phase change of ray 2 is made equal to zero), then the phase changes corresponding to rays 1 and 3 (ϕ_1 and ϕ_3) become

$$\phi_1 = 2k_f h \tag{13}$$

$$\phi_3 = 2k_f h - 2k_c h = 2h(k_f - k_c) = 4\pi hf\left(\frac{1}{\alpha_f} - \frac{1}{\alpha_c}\right) \tag{14}$$

In the above expressions ϕ_1 and ϕ_3 are in radians. If Φ_1 and Φ_3 are corresponding values in degrees, then

$$\phi_3 = \frac{\pi\Phi_3}{180} = 4\pi hf\left(\frac{1}{\alpha_f} - \frac{1}{\alpha_c}\right) \tag{15}$$

or

$$\Phi_3 = 720hf\left(\frac{1}{\alpha_f} - \frac{1}{\alpha_c}\right) \tag{16}$$

In the phase plot the variation corresponding to 0–360° is plotted in the gray scale from 0 to 256. Hence, if Φ_3 degree corresponds to an n gray scale value, then

$$n = (256\Phi_3)/360 \tag{17}$$

Hence, from the above two equations one can write (for a cell on substrate)

$$n = 512hf\left(\frac{1}{\alpha_f} - \frac{1}{\alpha_c}\right) \tag{18}$$

or

$$h = \frac{n}{512f\left(\frac{1}{\alpha_f} - \frac{1}{\alpha_c}\right)} \tag{19}$$

Clearly, if α_c is very close to α_f, then the denominator becomes very small and the cell thickness prediction becomes large.

In the amplitude image (the ultrasonic image generated by plotting the variation of the intensity of the reflected beam) the first dark interference ring, the one closest to the cell periphery, corresponds to a cell thickness of $\lambda_c/4 = \alpha_c/4f$, where λ_c is the wavelength inside the cell, and α_c and f are same as in Eq. 19. The second dark interference ring corresponds to a cell thickens of $3\lambda_c/4 = 3\alpha_c/4f$, and the mth ring corresponds to a cell thickens of $(2m - 1)\alpha_c/4f$. One can calculate the cell thickness from the mth interference ring and from the phase value at the same point and write

$$h = (2m - 1)\frac{\alpha_c}{4f} = \frac{n}{512f\left(\frac{1}{\alpha_f} - \frac{1}{\alpha_c}\right)} \tag{20}$$

From the above equation the following relation can be derived:

$$\alpha_c = \alpha_f + \frac{n\alpha_f}{128(2m - 1)} \tag{21}$$

From Eq. 21 one can easily obtain the longitudinal wave speed in the cell at the mth interference ring position. Note that in this manner the wave speed is obtained directly from the phase values without the use of any sophisticated inversion algorithm such as the simplex algorithm. However, this is only a rough estimate, because it assumes that the compressional wave speed does not vary from one point to the next. These rough estimates are used to define probable upper and lower bounds of the longitudinal wave speed in the cell.

EXPERIMENTAL RESULTS

Acoustic microscope-generated amplitude and phase images of a cell on silicon rubber and on a plastic substrate are shown in Figs. 5 and 6, respectively. These cells are XTH-2 cells, originating from *Xenopus* tadpole heart endothelium. Variations of the phase and amplitude values along any scan line in the image can be quantitatively recorded as shown in Fig. 5. Both phase and amplitude variations are plotted using a 256-level gray scale. In the phase image, a 256 gray scale variation corresponds to a phase difference of 360°. Several interference fringes can be seen in the amplitude image. However, in the phase image there is only one distinct jump of 256 gray scales, where the image changes from dark to bright.

One should note in the amplitude image of Fig. 5 that the reflected energy from the thin cell region is higher than that from the substrate. Similar results are obtained by model calculations by considering a thin liquid layer between the cell and the silicon rubber substrate (Fig. 3 *c*). Hence, to obtain the cell properties from these experimental data, one

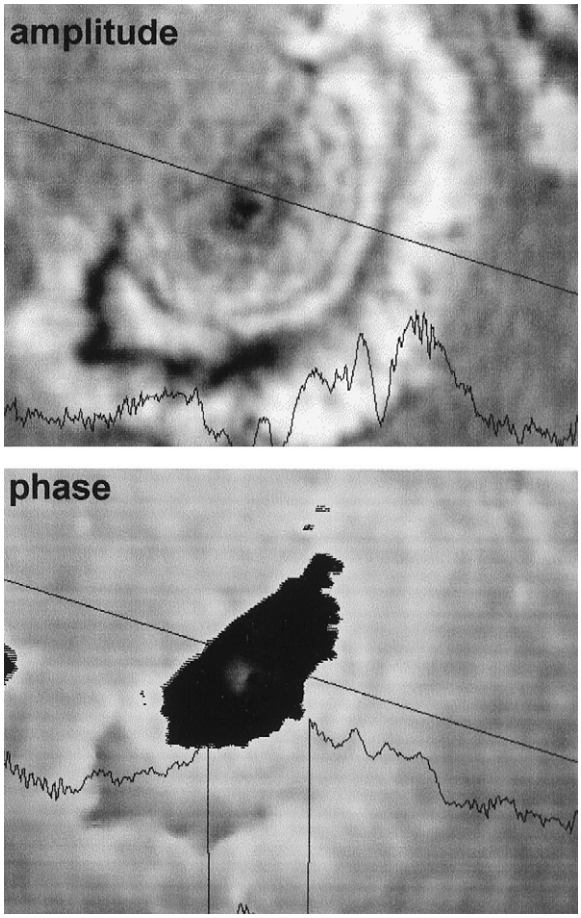

FIGURE 5 Acoustic microscope-generated amplitude (*top*) and phase (*bottom*) images of a cell on a silicon rubber substrate. Note that the brightness of some interferences exceeds that of the background.

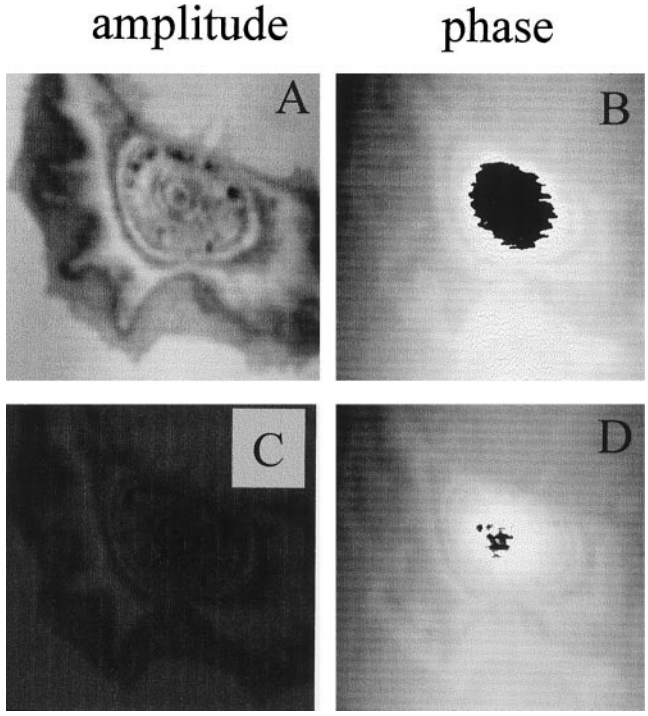

FIGURE 6 Amplitude (*A* and *C*) and phase (*B* and *D*) images of a cell, similar to that shown in Fig. 5, on the surface of a plastic Petri dish. The images have been taken at 0.98 (*A* and *B*) and 1.1 (*C* and *D*) GHz. Small differences in the position of the interference fringes are typical for pictures taken at different sound frequencies.

must consider the FSFS model. For the FSS model the cell region does not appear brighter than the substrate (see Fig. 3).

Before the amplitude and phase curves are inverted along a scan line, using the simplex algorithm (Kundu, 1991; Kundu et al., 1991) to obtain the cell properties, a rough estimate of the longitudinal wave speed in the cell is made using Eq. 21. This value is used to define probable upper and lower bounds of the wave speed in the cell. From the phase values, the cell thickness can be calculated in terms of the longitudinal wave speed (α) of the cell from Eq. 19. Bounds on the cell thickness are estimated in this manner; thus the need to estimate the cell thickness bounds by counting the interference rings is avoided. Several other improvements of the simplex inversion algorithm are incorporated into the present analysis. In the method published previously (Kundu et al., 1991, 1992) final results were obtained from one set of starting (or initial) values or, in other words, from only one simplex geometry. Sometimes this may cause convergence to a wrong set of values of the cell properties or parameters, when the estimates of probable and absolute bounds are not reasonably good.

Absolute bounds are the bounds of the parameters that must never be violated. Probable bounds lie within the absolute bounds. These bounds are thus narrower than the absolute bounds. When the probable bounds are selected, it is expected that the parameter values lie within these bounds. However, this requirement is not mandatory; simplex geometries or initial estimates of the cell parameters are obtained from the probable bounds. In the present analysis iterations are carried out with four different initial simplex geometries or four sets of initial guesses. Iterations are carried out to minimize the least-squares error between experimental $V(f)$ data and theoretical $V(f)$ values at every pixel point. After four sets of iterations, the converged values that produce minimum error are considered to be the final predictions of the cell properties. For most pixel points all four simplexes converge to the same predicted values. However, in some cases one or two simplexes converge to a different set of values. Comparing the errors from the four

TABLE 2 Absolute bounds of the unknown parameters

Unknown parameters	Upper bound	Lower bound
Wave speed (km/s)	2.1	1.5
Attenuation (a)	0.21	0.06
Liquid layer thickness (μm)	0.03	0.01

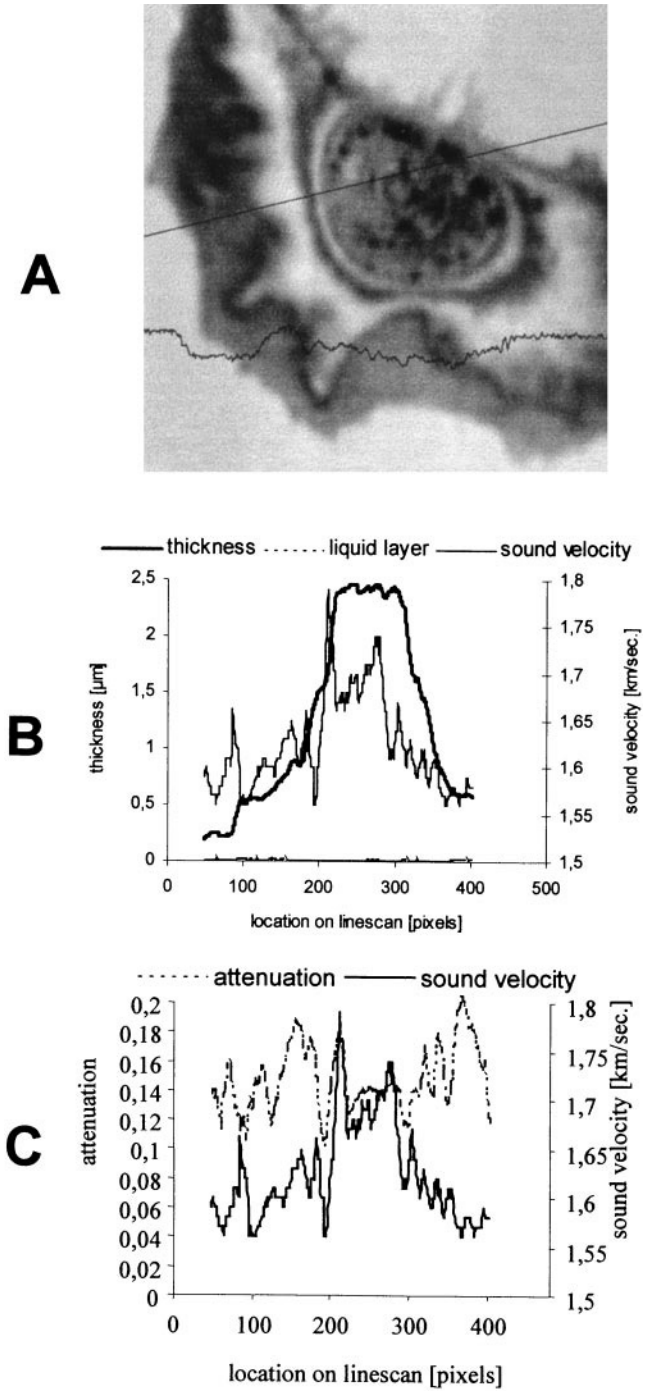

FIGURE 7 (*A*) Cell image. The straight line on the image is the scan line along which cell profiles and its properties are computed. (*B*) Predicted cell profile (*thick line*), wave speed (*thin line*), and liquid layer thickness (*dotted line*) variation along the scan line. (*C*) Predicted wave speed (*continuous line*) and attenuation (*dotted line*) variation along the scan line.

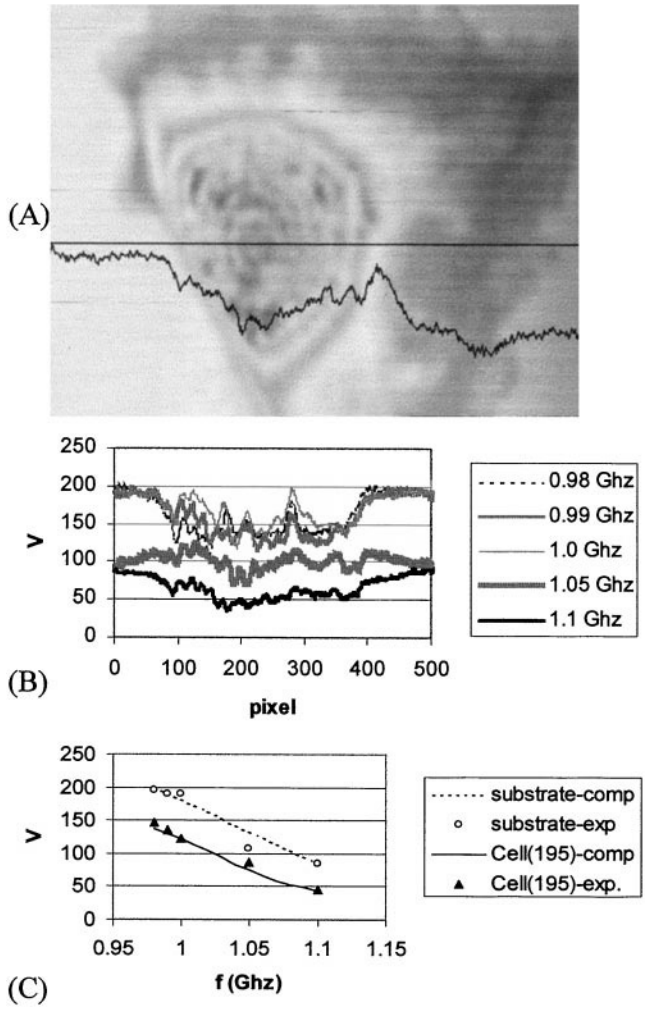

FIGURE 8 (*A*) Cell image. The straight line on the image is the scan line along which cell profiles and its properties are computed. (*B*) $V(x)$ curves along the scan line (after correction for the substrate inclination) for four different frequencies: 0.98, 0.99, 1.0, 1.05, and 1.1 GHz. (*C*) Experimental (*markers without connecting lines*) and theoretical (*lines without markers*) $V(f)$ curves for the substrate and for the cell on substrate at pixel position 195. Theoretical $V(f)$ curves have been obtained for the cell profile and cell properties shown in Fig. 9.

sets of converged values, the computer program picks the set that produces the minimum error as the final predicted values of the cell parameters.

The cell properties that are calculated in this manner are longitudinal wave speed (α), attenuation (a), and cell thickness (h). In addition to these three unknowns, the liquid layer thickness (t) between the cell and the substrate is also considered as the fourth unknown quantity. The cell density is assumed to be 1.06 g/cm^3. Other cell properties are computed by the simplex inversion algorithm giving the absolute bounds in Table 2.

Using these bounds, we calculate the cell properties (shown in Fig. 7). Fig. 7 *A* shows the amplitude image of the cell; the straight line in this image is the scan line along which the cell properties are computed. The predicted cell profile, wave speed, and attenuation variation in the cell along the scan line are shown in Fig. 7, *B* and *C*. It is interesting to see that the wave speed increases from the cell periphery toward the cell center, and it drops slightly at the

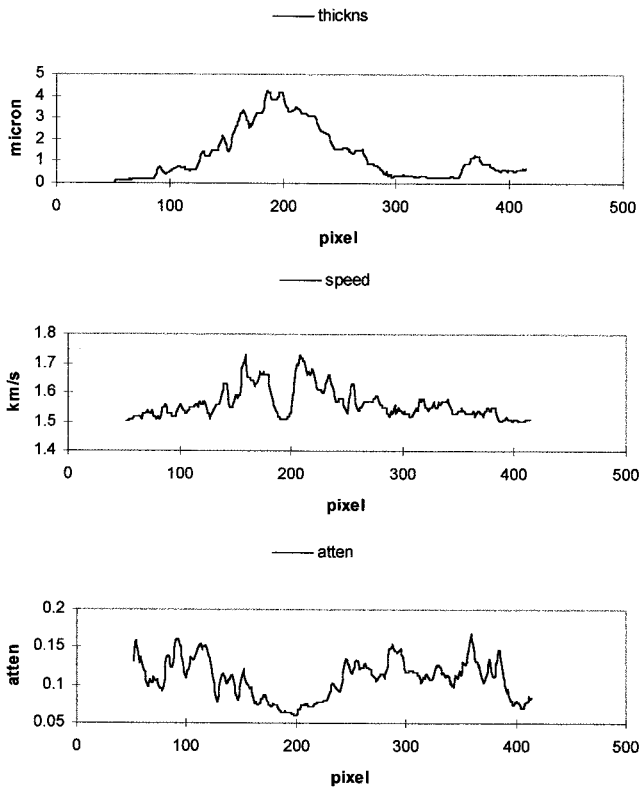

FIGURE 9 Cell profile (*top figure*), P-wave speed (*middle figure*), and attenuation (*bottom figure*) variation in the cell along the scan line, shown in the acoustic image of the cell in Fig. 8 *A*.

nucleus region. On the other hand, the attenuation is high near the cell periphery and low in the central portion. Variations in the thickness of the very thin liquid layer between the cell and the substrate are also shown by the thin dotted line near the horizontal axis of Fig. 7 *B*.

An amplitude image of a second XTH-2 cell on a silicon substrate is shown in Fig. 8 *A*. The straight scan line and the nonlinear voltage variation along the scan line or the $V(x)$ curve are also plotted on the image. The difference in the voltage values over the substrate region on the left and right sides of the cell is due to the slight inclination of the substrate plate. It is also evident in the acoustic image. The left side of the substrate image appears brighter than the right side. $V(x)$ curves for different frequencies (0.98, 0.99, 1.0, 1.05, and 1.1 GHz) are shown in Fig. 8 *B*. The substrate inclination error has been corrected in these curves.

The $V(f)$ curve at any pixel position can be generated from the $V(x)$ values at different frequencies for that pixel position. Experimental $V(f)$ values over the substrate and the cell (pixel position 195) are shown in Fig. 8 *C* by circles and triangles, respectively. Theoretical $V(f)$ curves (obtained from the predicted cell properties) over the same two regions are shown by dotted and continuous lines, respectively, in Fig. 8 *C*. The least-squares error is computed from the mismatch between the theoretical and experimental values. By minimizing this error we predicted the cell dimensions and cell properties.

Predicted cell profile, P-wave speed, and attenuation variations along the scan line of this cell are shown in Fig. 9.

CONCLUDING REMARKS

It is shown in this paper that the cell properties and the cell thickness profiles can be obtained from the $V(f)$ curve (voltage versus frequency curve) generated by an acoustic microscope. Longitudinal wave speed and attenuation variation in a cell, predicted in this manner, are justified in a qualitative manner. This technique has the potential of replacing the $V(z)$ (voltage versus defocus distance) technique because experimentally it is easier and quicker to generate $V(f)$ curves than it is to generate $V(z)$ curves.

We thank Dr. von der Burg (Leipzig) for the determination of sound speed in silicon rubber.

The financial support provided by the Alexander von Humboldt Foundation of Germany to the first author, by the Gesellschaft der Freunde und Förderer der Johann Wolfgang Goethe Universität, and by the Deutsche Forschungsgemeinschaft to JB-H (Schwerpunkt: "Neue mikroskopische Methoden in Biologie und Medizin" Be 423/16) is gratefully acknowledged.

REFERENCES

Bereiter-Hahn, J. 1976. Dimethylaminostyrylmethylpyridiniumiodine (DASPMI) as a fluorescent probe for mitochondria in situ. *Biochim. Biophys. Acta.* 423:1–14.

Bereiter-Hahn, J. 1995. Probing biological cells and tissues with acoustic microscopy. *Adv. Acoustic Microsc.* 1:79–115.

Bereiter-Hahn, J., C. H. Fox, and B. Thorell. 1979. Quantitative reflection contrast microscopy of living cells. *J. Cell Biol.* 82:767–779.

Bereiter-Hahn, J., and H. Lüers. 1994. The role of elasticity in the motile behaviour of cells. *NATO ASI Ser H Cell Biol.* 84:181–230.

Bereiter-Hahn, J., and H. Lüers. 1998. Subcellular tension fields and mechanical resistance of the lamella front related to the direction of locomotion. *Cell Biochem. Biophys.* 29:243–262.

Bereiter-Hahn, J., C. Stübig, and V. Heymann. 1995. Cell cycle-related changes in F-actin distribution are correlated with glycolytic activity. *Exp. Cell Res.* 218:551–560.

Chubachi, N., K. Hiroshi, S. Toshio, and T. Wakahara. 1992. Acoustic microscope for measuring acoustic properties by micro-defocusing method. *In* Acoustical Imaging, Vol. 19. H. Ermert and H.-P. Harjes. 685–689.

Duszyk, M., B. Schwab, G. I. Zahalak, H. Qian, and E. L. Elson. 1989. Cell poking: quantitative analysis of indentation of thick viscoelastic layers. *Biophys. J.* 55:683–690.

Ghosh, T., K. I. Maslov, and T. Kundu. 1997. A new method for measuring surface acoustic wave speeds by acoustic microscopes and its application in characterizing laterally inhomogeneous materials. *Ultrasonics.* 35:357–366.

Goldmann, W. H., R. Galneder, M. Ludwig, W. M. Xu, E. D. Adamson, N. Wang, and R. M. Ezzell. 1998. Differences in elasticity of vinculin-deficient F9 cells measured by magnetometry and atomic force microscopy. *Exp. Cell Res.* 239:235–242.

Grill, W., K. Hillmann, K. U. Würz, and J. Wesner. 1996. Scanning ultrasonic microscopy with phase contrast. *In* Advances in Acoustic Microscopy, Vol. 2. A. Briggs and W. Arnold, editors. Plenum Press, New York. 167–218.

Harris, A. K. 1982. Traction and its relation to contraction in tissue cell locomotion. *In* Cell Behaviour. R. Bellairs, A. Curtis, and G. Dunn, editors. Cambridge University Press, New York. 109–134.

Harris, A. K., P. Wild, and D. Stopak. 1980. Silicon rubber-substrata: a new wrinkle in the study of cell locomotion. *Science.* 208:177–179.

Hassan, E., W. F. Heinz, M. D. Antonik, N. P. DCosta, S. Nageswaran, C. A. Schoenenberger, and J. H. Hoh. 1998. Relative microelastic mapping of living cells by atomic force microscopy. *Biophys. J.* 74: 1564–1578.

Hildebrand, J. A., and D. Rugar. 1984. Measurement of cellular elastic properties by acoustic microscopy. *J. Microsc.* 134:245–260.

Hildebrand, J. A., D. Rugar, R. N. Johnston, and C. F. Quate. 1981. Acoustic microscopy of living cells. *Proc. Natl. Acad. Sci. USA.* 78: 1656–1660.

Hillmann, K., W. Grill, and J. Bereiter-Hahn. 1994. Determination of ultrasonic attenuation in small samples of solid material by scanning acoustic microscopy with phase contrast. *J. Alloys Compounds.* 211/212: 625–627.

Hiramoto, Y. 1987. Evaluation of cytomechanical properties. *In* Cytomechanics. J. Bereiter-Hahn, O. R. Anderson, and W.-E. Reif, editors. Springer-Verlag, Berlin, Heidelberg, and New York. 31–46.

Izzard, C. S. 1976. Cell-to-substrate contacts in living fibroblasts: an interference reflexion study with an evaluation of the technique. *J. Cell Sci.* 21:129–159.

Karl, I., and J. Bereiter-Hahn. 1999. Tension modulates cell surface motility. *Cell Motil. Cytoskeleton.* (in press).

Kundu, T. 1991. Inversion of acoustic material signature of multilayered solids. *J. Acoust. Soc. Am.* 91:591–600.

Kundu, T., J. Bereiter-Hahn, and K. Hillmann. 1991. Measuring elastic properties of cells by evaluation of scanning acoustic microscopy V (Z) values using simplex algorithm. *Biophys. J.* 59:1194–1207.

Kundu, T., J. Bereiter-Hahn, and K. Hillmann. 1992. Calculating acoustical properties of cells: influence of surface topography and liquid layer between cell and substrate. *J. Acoust. Soc. Am.* 91:3008–3017.

Litniewski, J., and J. Bereiter-Hahn. 1990. Measurements of cells in culture by scanning acoustic microscopy. *J. Microsc.* 158:95–107.

Litniewski, J., and J. Bereiter-Hahn. 1992. Acoustic velocity determination in cytoplasm by $V(z)$ shift. *In* Acoustical Imaging, Vol. 19. H. Ermert and H.-P. Harjes, editors. 535–538.

Nagy, P. B., and L. Adler. 1990. Acoustic material signature from frequency analysis. *J. Appl. Phys.* 67:3876–3878.

Radmacher, M., M. Fritz, C. Kacher, J. Cleveland, and P. Hansma. 1996. Measuring the viscoelastic properties of human platelets with the atomic force microscope. *Biophys. J.* 70:556–567.

Sasaki, H., M. Tanaka, Y. Saijo, H. Okawai, Y. Terasawa, S. Nitta, and K. Suzuki. 1996. Ultrasonic characterisation of renal cell carcinoma tissue. *Nephron.* 74:125–130.

Sarvazyan, A., A. Scovoroda, and D. Vucelic. 1992. Utilisation of surface acoustic waves and shear acoustic properties for imaging and tissue characterisation. *In* Acoustical Imaging, Vol. 19. H. Ermert and H.-P. Harjes, editors. 463–468.

Schmid-Schönbin, G. W. 1990. Leukocyte biophysics. An invited review. *Cell Biophys.* 17:107–135.

Ziemann, F., J. Radler, and E. Sackmann. 1994. Local measurements of viscoelastic moduli of entangled actin networks using an oscillating magnetic bead micro-rheometer. *Biophys. J.* 66:2210–2216.